Remote Sensing of Environment 239 (2020) 111607



Contents lists available at ScienceDirect

Remote Sensing of Environment

journal homepage: www.elsevier.com/locate/rse



Characterization of rain impact on L-Band GNSS-R ocean surface measurements



Rajeswari Balasubramaniam*, Christopher Ruf

University of Michigan, Ann Arbor, MI, United States of America

ARTICLE INFO

Edited by Menghua Wang

Keywords:
CYGNSS
GNSS-R
Radar cross-section
Rain

ABSTRACT

Earth remote sensing using reflected GNSS signals is currently an emerging trend especially in ocean surface wind measurements. Unlike the existing scatterometer missions, GNSS-R uses L-Band navigation signals that can penetrate through clouds and rain. Rain may have a negligible impact on the transmitted signal in terms of path attenuation at this wavelength. However, there are other effects due to rain, such as changes in surface roughness and rain induced local winds, which can significantly alter the measurements. Currently, there is no observation-based characterization of all possible impacts of rain on radar forward scatter, which is the nature of operation of GNSS-R missions. In this study, we propose a 3-fold rain model which accounts for attenuation, surface effects of rain and rain induced local winds. We utilize the large dataset of measurements made by the CYGNSS mission to separate these different effects of rain. The attenuation model suggests that a total of at least 96% transmissivity exists at L-Band up to a rain rate of 30 mm/h. A perturbation model is used to characterize the other rain effects. It suggests that rain is accompanied by an overall reduction in the scattering cross-section of the ocean surface and, most importantly, this effect is observed only up to surface wind speeds of 15 m/s, beyond which the gravity capillary waves dominate the scattering in the quasi-specular direction. Observations also suggest that, at very low wind speeds, the lower bound on wavenumber of the portion of the surface roughness spectrum that influences the measurements deviates from the geometric optics approximation normally used. This work binds together several rain-related phenomena and enhances our overall understanding of rain effects on GNSS-R measurements.

1. Introduction

For several decades, scatterometers have provided valuable ocean surface wind information by measuring the back-scattering properties of the surface. The sensitivity to wind in such measurements is due to Bragg scattering from the wind-driven centimeter scale capillary waves. The presence of rain, perturbing the measured radar cross-section, affects about 7% of global scatterometer measurements (Weissman et al., 2012). Interesting meteorological phenomena are often accompanied by the presence of rain, so understanding its influence on the measurements is critical. There have been many studies that show the rain contamination of scatterometer winds (Tang et al., 2013, 2015).

When raindrops strike a water surface, the disturbance creates a central column of water referred to as a stalk and a ring of waves that propagate radially out from the point of impact (Craeye et al., 1997). Several studies on the surface effects of rain suggest that at microwave frequencies the dominant surface features, when viewed at oblique angles of incidence, are the ring waves generated by raindrops hitting the water surface and, at grazing incidence angles, the stalks (Bliven et al., 1997; Craeye et al., 1997; Wetzel, 1990; Bass et al., 1968). Craeye et al. (1997) have provided a ring-wave spectrum for rain simulated using in-situ experiments over a broad range of rain rates from 5 to 200 mm/h. This ring-wave spectrum has been widely used to account for the effects of rain in scatterometric measurements (Xu et al., 2014; Zhang et al., 2016). There have also been many physics based and empirical models of rain effects from C to Ku band (Nielsen and Long, 2008; Stiles and Yueh, 2002; Draper and Long, 2004; Contreras and Plant, 2006).

Global Navigation Satellite System-Reflectometry (GNSS-R) offers an alternative approach to measure ocean surface wind speed (Clarizia et al., 2009; Ruf et al., 2013; Foti et al., 2015; Soisuvarn et al., 2016). GNSS-R measures reflected GPS signals to extract useful remote sensing information about the reflecting surface. GNSS-R sensors operate in bistatic mode, with the transmitter on the Global Positioning System (GPS) satellite or other navigation platforms. GNSS-R ocean wind measurements are similar to scatterometers in that they are also

* Corresponding author.
E-mail address: rajibala@umich.edu (R. Balasubramaniam).

https://doi.org/10.1016/j.rse.2019.111607
Received 2 July 2019; Received in revised form 30 November 2019; Accepted 12 December 2019
0034-4257/ © 2020 The Authors. Published by Elsevier Inc. This is an open access article under the CC BY license (http://creativecommons.org/licenses/BY/4.0/).

sensitive to the ocean surface roughness caused by winds, except in the quasi-specular forward scattering direction (Zavorotny and Voronovich, 2000).

There have been some initial studies of the effects of rain on GNSS-R measurements for altimetry and ocean wind measurements (Asgarimehr et al., 2018; Ghavidel and Camps, 2016). For instance, Asgarimehr et al. (2018) detect around 0.7 dB drop in the magnitude of the Normalized Bistatic Radar Cross-Section from TDS-1 measurements (Foti et al., 2015). However, due to the limited availability of data, there have so far been no clear conclusions drawn about the different impacts of rain on the GNSS-R measurements. There have also been theoretical simulations of the rain effects on the ocean surface to account for the splash effect (Zavorotny and Voronovich, 2018) and to account for attenuation effects (Asgarimehr et al., 2019). Zavorotny and Voronovich (2018) show that the splash effect is visible only at very low wind speeds (< 5 m/s) where specular scattering can be observed and Asgarimehr et al. (2019) have shown that the total attenuation effect on retrieved wind speed is very small. With the onset of the Cyclone Global Navigation Satellite System (CYGNSS) mission, a large number of GNSS-R measurement samples is now available on a global scale which encompasses a wide range of wind speeds and rain rates. This has enabled the possibility to analyze and understand the individual effects of rain on GNSS-R measurements more comprehensively.

CYGNSS is a LEO GNSS-R constellation which was launched in 2016 to measure ocean surface winds especially in tropical cyclones (Ruf et al., 2018). It operates at the all-day all-weather GPS L1 frequency (1.575 GHz) to measure the Normalized Bistatic Radar Cross-Section (σ_0) of the ocean surface. Though the L-Band signals can penetrate through clouds and rain, under very heavy precipitation there are other surface effects of rain that can affect the measurements (Balasubramaniam and Ruf, 2018). The CYGNSS observatories carry a passive instrument called the Delay Doppler Mapping Instrument (DDMI) that resolves the received reflected-GPS signals into delay-Doppler space. This delay-Doppler representation of the received power signal is called a Delay-Doppler Map (DDM). Each DDMI outputs 4 DDMs per second thereby making a total of 32 sea-surface measurements globally every second (Ruf et al., 2016). The received DDMs undergo Level-1 calibration to derive the σ_0 which is then mapped to wind speed using a Geophysical Model Function (GMF) (Ruf and Balasubramaniam, 2018).

This paper is broadly divided into the following sections:Section 2 describes the models proposed to account for different effects of rain. Section 3 uses the CYGNSS observations to empirically characterize the perturbations in σ_0, followed by the Results section, where a comparison of model and observation-based inferences are made. Finally, the paper concludes with Discussion and conclusions, where key observations are reiterated, and their physical implications discussed.

2. Theoretical model

The effects of rain on the GNSS-R forward scatter signal can be broadly divided into 3 major components. First is the path attenuation of the propagating signal. Second is raindrops splashing on the water surface, modifying the ocean surface roughness. Third is precipitation causing locally generated winds by pushing down the air column. In this work, we try to incorporate physics-based principles and direct observations to model each of these effects. Fig. 1 is the proposed rain model used to account for these effects. GPS satellites transmit L1 C/A navigation signals (1.575 GHz) from a Medium Earth Orbit (MEO) at approximately 20,200 km altitude. These signals are scattered from the ocean surface and received by the CYGNSS observatories in Low Earth Orbit (LEO) at an altitude of approximately 520 km. In the event of rain, attenuation occurs along two paths, first as the GPS signal propagates from the freezing level to the ocean surface. The signal is then scattered from the surface of the ocean, with its scattering cross-section dependent on the roughness of the surface. The surface is perturbed by the falling rain drops in two ways. At very low wind speeds (near specular scattering regime), a rain drop hitting the surface can cause modifications to the roughness spectrum. This effect becomes negligible when the surface roughness is dominated by wind generated capillary waves (diffused scattering regime). At higher rain rates, the rain can also induce localized winds by pushing down the air column (Weissman et al., 2012). The reflected L1 signal is then attenuated a second time along its return path towards the CYGNSS observatory. Fig. 2 gives a pictorial representation of this sequence of interactions.

2.1. Radiative transfer model for propagation loss

Absorption of the GPS signal along its propagation path can be modelled using the radiative transfer equation. Let L_a represent the transmissivity of the medium between the transmitter and the surface. For a plane wave, the transmissivity is the negative exponential of the optical depth. The optical depth τ_p can be realized as the slant path integration of specific absorption from the surface up to the freezing level. The integration height used here is the average height of the freezing level in the tropics which is approximately 4800 m (Harris Jr et al., 2000). The model for absorption due to hydrometeors is derived using a regression analysis from Ulaby et al. (2014). The equations governing propagation path loss are given by Eq. (1), Eq. (2), Eq. (3):

$$L_a = \exp(-\tau_p) \tag{1}$$

$$\tau_p = \int_0^{Z_L sec(\theta)} \alpha_p(z)dz \tag{2}$$

$$\alpha_p = \alpha_1(f)R^{b(f)} \tag{3}$$

where f is the frequency in GHz, R is the rain rate in mm/h and $\alpha_1(f)$ and $b(f)$ are regression-based model coefficients given by Ulaby et al. (2014), Eq. (4), Eq. (5):

$$\alpha_1(f) = 6.39*10^{-5}f^{2.03} \tag{4}$$

$$b(f) = 0.851f^{0.158} \tag{5}$$

These expressions are valid for frequencies up to 2.9 GHz and therefore can be used at the GPS L1 frequency of 1.575 GHz. The double-path integrated loss is shown as a function of rain rate in Fig. 3.

The model indicates that there is a total transmissivity of $> 96\%$ up to 30 mm/h. This model re-attests to the fact that rain has negligible attenuation up to 30 mm/h for GPS signals. The modified bistatic scattering forward model, including the double-path attenuation due to rain, is given by Eq. (6).

$$P_G(t,f) = T_i^2 \frac{P_T\lambda^2}{(4\pi)^3}^2{}_a \int\int \frac{G_T(\vec{\rho})G_R(\vec{\rho})F(\vec{\rho})\Lambda^2(t,\vec{\rho})|S(\vec{\rho})|^2\sigma_0^{obs}(\vec{\rho})}{r_0^2(\vec{\rho})r^2(\vec{\rho})}d^2\vec{\rho} \tag{6}$$

where L_a^2 is the transmissivity accounting for rain attenuation. $P_G(\tau,f)$ is the coherently processed scattered signal power at time delay τ and Doppler shift f over the coherent integration time T_i. P_T,λ and G_T are the GPS transmit power, carrier wavelength and antenna gain respectively. r_0 and r are the transmitter-to-surface and surface-to-receiver ranges respectively. G_R is the CYGNSS receiver antenna gain and σ_0 is the Normalized Bistatic Radar Cross-Section. Λ and S represent the GPS spreading function and the Doppler zone function of the GPS respectively. The attenuation corrected normalized bistatic radar cross-section, $\sigma_0^{obs}|_R$ in linear scale can be derived by inverting the above model, or

$$\sigma_0^{obs}|_R = \frac{P_G(4\pi)^3 r_0^2 r^2}{P_T\lambda^2 G_T G_R}\frac{1}{L_a^2} \tag{7}$$

Path attenuation due to rain at microwave frequencies plays a minor role in the change in radar cross-section. However, properly correcting

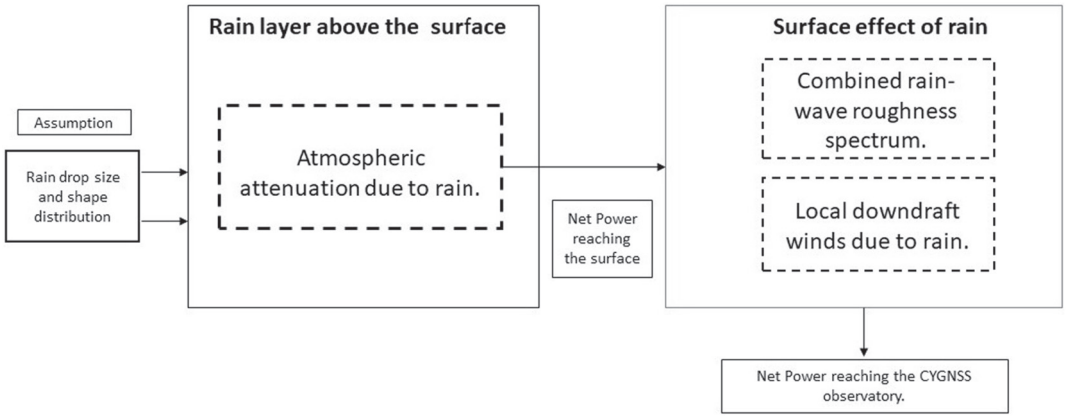


Fig. 1. Model for the effects of rain on GNSS-R measurements.

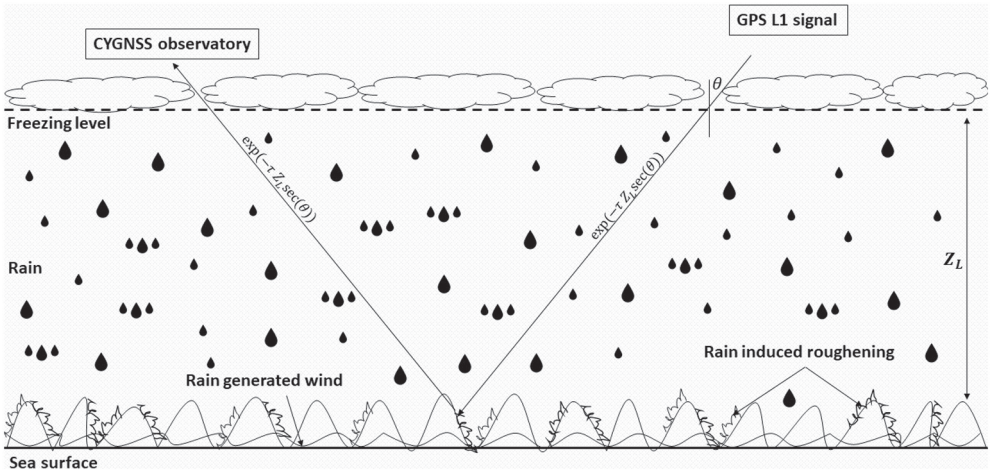


Fig. 2. Modifications of the received reflected signals through rain.

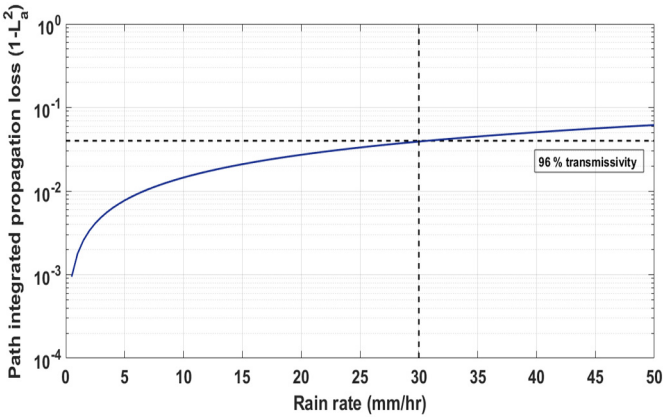


Fig. 3. Path integrated propagation loss.

for its effect will help accurately characterize the other, more dominant, components such as modification to surface roughness and local downdraft winds created by the rain.

2.2. Modelling surface effects of rain

The global distribution of wind speeds over the ocean has a mean in the range of 6–8 m/s. Based on the wind speed, a fully developed ocean wind-wave spectrum can be broadly broken down into 2 regimes of electromagnetic scattering. The first is the near specular regime, for which wind speeds are generally < 5 m/s, which has a surface Rayleigh parameter much less than 1. Second is the diffuse scattering regime, with wind speeds ≥5 m/s, in which very large surface Rayleigh parameters hold and where the geometric optics approximation is valid (Voronovich and Zavorotny, 2017; Zavorotny and Voronovich, 2018). In the diffuse scattering regime, surface roughness due to wind-wave interactions dominates over rain induced roughness. The induced surface roughness due to a rain drop hitting the water surface is dominant only at low wind speeds (< 5 m/s) (Zavorotny and Voronovich, 2018).

A rain drop hitting the water surface causes 3 major types of surface deformation — crater, crown and stalk. First, a cavity on the water surface is formed along with a crown which then changes into a vertical stalk of water that finally subsides to generate rings of gravity capillary waves (Bliven et al., 1997). The dominant features in this process with respect to microwave frequencies are the stalks and the ring waves. At oblique incidence angles, the cm-wavelength ring waves play the dominant role while the stalks play a dominant role only at grazing angles (Craeye et al., 1997).

The approach used to model the water surface impact of raindrops follows the widely used idea (Craeye et al., 1997) of first order superposition of the rain generated ring-wave spectrum and the wind-forced Elfouhaily elevation spectrum (Elfouhaily et al., 1997). The ring-wave spectrum is a log-Gaussian model of the form Eq. (8):

$$S(k) = \frac{1}{2\pi} v_{gr}(k) S_{peak} \exp\left(-\pi \frac{\ln\left(\frac{f(k)}{f_p}\right)}{\frac{\Delta f}{f_p}} \right) \tag{8}$$

where v_{gr} is the group velocity in m/s, S_{peak} is the power law spectral

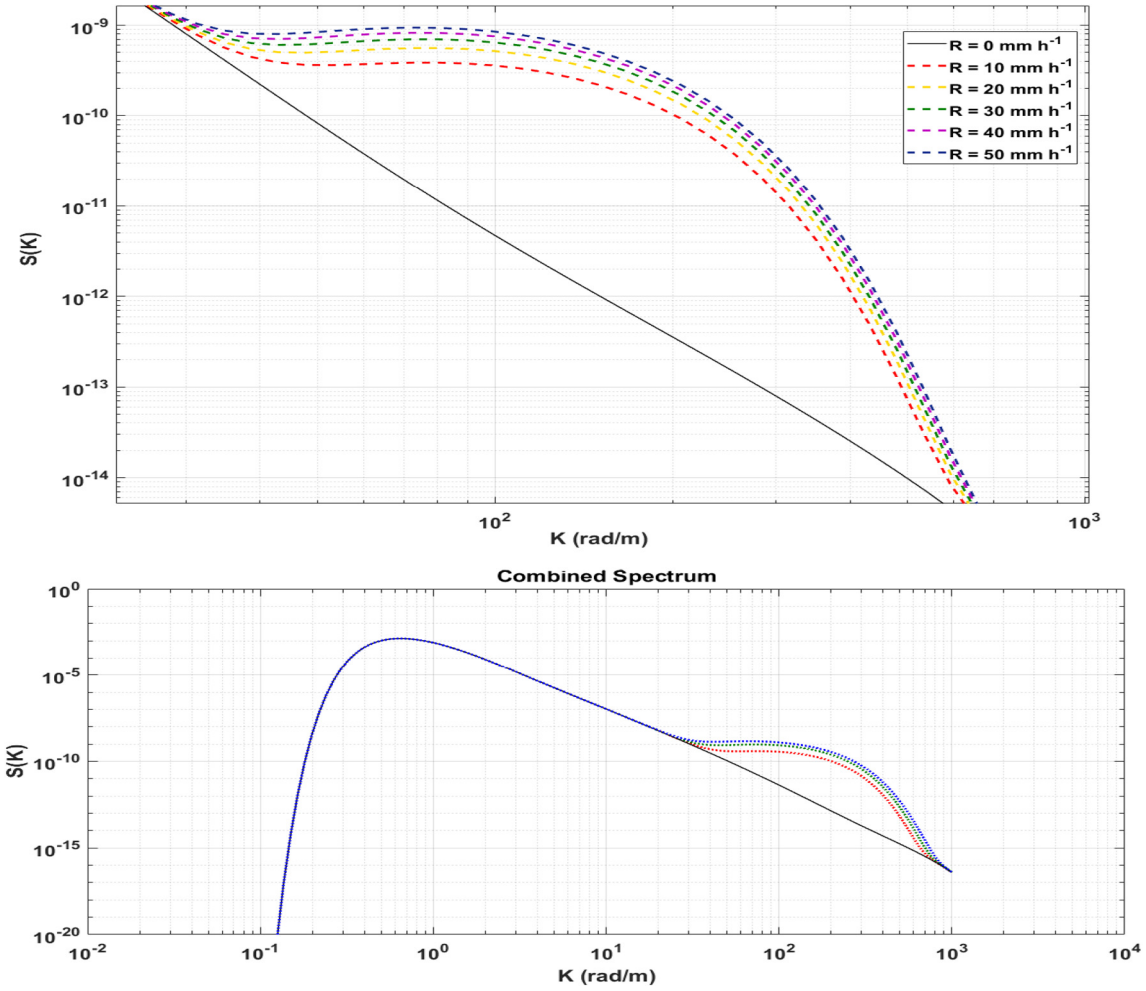


Fig. 4. Superposition of Elfouhaily and ring-wave spectra to generate the combined rain-wind roughness spectrum for 5 different rain rates and a wind speed = 5 m/s. (top) Closeup of portion of the spectrum affected by rain. (bottom) Full spectrum including the dominant lower wind roughened portion.

model given by $6 * 10^{-4}R^{0.53}$, $f(k)$ can be derived from the dispersion relation $w^2 = gk + hk^3$. $\Delta f = 4.42 + 0.0028R$ Hz, $f_p = 5.772 - 0.0018R$ Hz. These model coefficients were estimated in Craeye et al. (1997) for ring waves of wavelengths of 1.94 –20.8 cm.

The resulting combined rain-wind spectrum for an example wind speed of 5 m/s and different rain rates is shown in Fig. 4. The wave spectrum describes the distribution of energy at different wavenumbers. The Elfouhaily wind-wave spectrum has its peak between 10^{-1} and 1 rad/m waves and the ring-wave spectrum has its peak between 100 and 300 rad/m. Larger wavenumbers represent shorter waves — thus, the ring waves introduce additional short-scale roughness over the long scale roughness induced by wind. The GNSS-R σ_0 observations are inversely proportional to the mean square slope of the surface. The mean square slope is the integral of the omnidirectional slope spectrum (Elfouhaily et al., 1997) up to a cut-off wave number which is typically determined using the geometric optics approximation for electromagnetic scattering. At the GNSS-R L-Band wavelength, the cut-off wavenumber is approximately 10–12 rad/m. Note that the portion of the roughness spectrum that is perturbed by rain is predominantly above this cut-off. The implications of this relationship are addressed in detail in Section 4 below.

2.3. Rain induced local winds

In addition to the signal attenuation effect of rain and the rain induced surface roughness due to the drop-splash effect, rain induced local winds can be generated by the downdraft of the air column below a rain cell. This downdraft can alter the surface wave spectrum by raising the near-surface wind speed due to outflow (Weissman et al., 2012). Accurate understanding of this effect entails the consideration of various physical processes together. The end goal of this sub-section is to derive a physics-based relationship between surface rain rate and its induced downdraft winds. The proposed algorithm to calculate the downdraft winds is represented in Fig. 5.

We first derive the drop size distribution of the raindrops using the widely used Marshall-Palmer exponential rain drop distribution

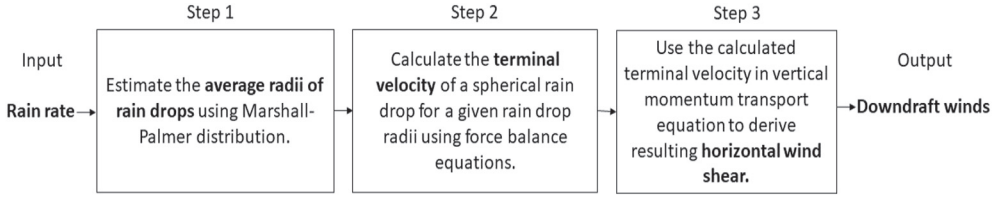


Fig. 5. Algorithm to calculate rain induced local winds.

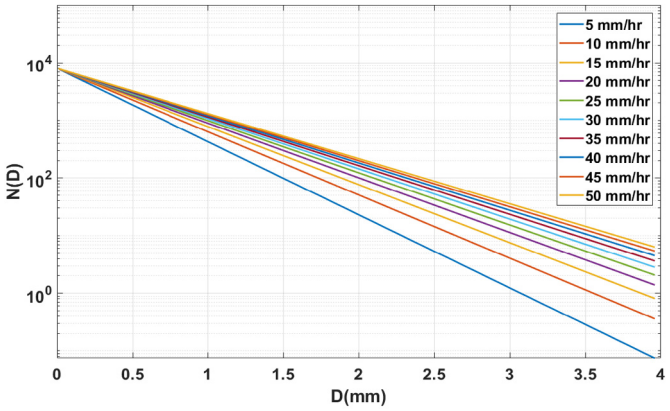


Fig. 6. Marshall-Palmer distribution based weighed average estimate of rain drop radii.

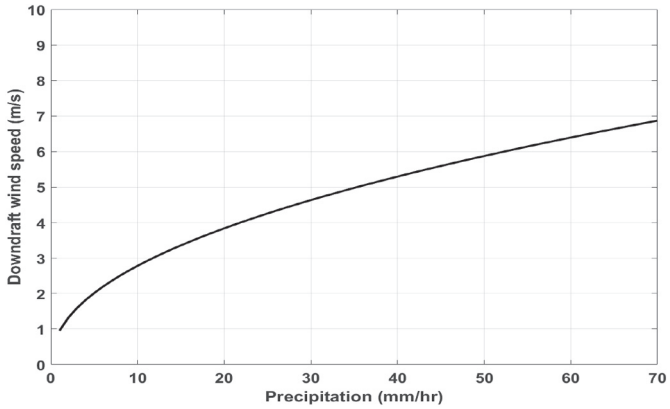


Fig. 7. Downdraft windspeed model.

(Marshall and Mc. K. Palmer, 1948). This distribution provides an empirical relationship between rain rate and rain drop size distribution as given by Eq. (9):

$$N_D = N_0 \exp(-\lambda D)$$
$$\lambda = 41R^{-0.21}\ \text{cm}^{-1} \tag{9}$$

where N_D is the drop number density for a given diameter of rain drop, D, and rain rate, R. The number density distribution derived from the above expression is shown in Fig. 6. The size of the rain drops varies between 0.01 mm and 4 mm, above which surface tension weakens compared to gravity and the drop splits into smaller sizes. An important assumption made while using the Marshall-Palmer distribution is that the variation in drop size distribution with cloud type and geographic region introduce only second order variability relative to the other major effects described here. Using this density distribution, the half order moment of the radius of the rain drop, required to compute the terminal velocity of the falling rain drops, can be derived as a function of rain rate.

The terminal velocity of the falling raindrops is computed using an empirical power law model (Atlas and Ulbrich, 1977; Doviak et al., 2006), as given by Eq. (10):

$$v(D) = 386.6D^{0.67} \tag{10}$$

where D is the rain drop diameter in meters and v is the terminal velocity. Terminal velocity can be solved from the above equation by using twice the half order moment of the radius derived from the Marshall-Palmer distribution for the diameter in the above equation.

The derived terminal velocity can now be used in the momentum conservation equations (Holleman, 2001) to calculate the rain induced downdraft wind speed. The model relating the downdraft wind speed to the surface rain rate derived using the above method is depicted in Fig. 7.

It can be observed from this model that downdraft winds increase monotonically with rain rate, as expected. This model provides an accounting for the excess wind generated due to rain, and thus for the change in radar cross-section due to rain-induced downdrafts. In the later sections, we evaluate how this physically based model compares to CYGNSS radar cross-section measurements.

3. Observations

3.1. Data description

We consider various statistical analyses of CYGNSS data to identify and characterize the rain signature in its measurements. The data used are the *v*2.1 release of CYGNSS Level 1 σ_0 measurements and Level 3 wind retrieval from all 8 CYGNSS observatories over a period of 200 days between DOY 77 and DOY 276 of 2017. The data are matched to the European Numerical Weather Prediction Model, ECMWF 10 m referenced re-analysis ocean surface wind speeds at the specular point for ground truth wind speed. ECMWF wind speed information is matched to CYGNSS specular point locations through bi-linear interpolation in space and linear interpolation in time (Ruf and Balasubramaniam, 2018). The data source used for precipitation information is the Integrated Multi-satellitE Retrieval for GPM (IMERG) *V* 05*B* half hourly final run gridded data product with a spatial resolution of 0.1 × 0.1 deg and temporal resolution of 30 min (Huffman et al., 2015). The pertinent CYGNSS data products are provided in Table 1 (Ruf et al., 2016). The GPM measurements are re-gridded to match the Level 3 CYGNSS gridded data product which has a spatial resolution of 0.2 × 0.2 deg, a temporal resolution of 60 min, and are collocated to the nearest CYGNSS specular point DDM in space and time Ruf et al., 2016. The precipitation information is also matched to the Level 3 CYGNSS gridded wind speed product to observe the global probability density function (pdf) of CYGNSS winds under low and high precipitation conditions.

The CYGNSS Level 1 σ_0 data are filtered by several quality measures for this analysis. Only data with a very high antenna gain (> 10 dB) are used. The overall quality flag of the Level 1 data is set to best quality with a filter to exclude GPS block type *IIF* measurements to ensure best quality CYGNSS measurements. The sample population for this analysis contains approximately 10^8 measurements.

3.2. Controlled CYGNSS-GPM dataset

In addition to the large CYGNSS-GPM dataset described above, a second control dataset containing 110 individual CYGNSS tracks was generated to test and understand the behavior of σ_0 in the presence of rain. In addition to being passed through the aforementioned quality tests, these CYGNSS tracks are subjected to additional control over various surface properties and satellite geometries (all the tracks are provided in Appendix B). Each CYGNSS track is an overpass by a single CYGNSS observatory over a contiguous strong rain event followed by a rain-free portion. Here, strong rain events are identified as events with peak rain rates > 30 mm/ h. This value of rain rate is chosen to correspond to situations where the attenuation effect of rain begins to become significant. It is important to have both strong rain and no-rain conditions present in the same track in order to study variations in σ_0 under similar measurement conditions.

The control parameters for the surface properties are the Significant Wave Height (SWH) and wind conditions along the track between the peak-rain and no-rain regions. SWH controls for the presence of swell effects. For SWH, WaveWatch III IFREMER SWH information is used and, for wind speed, ECMWF 10 m surface wind speed information is used. The control parameters for satellite geometry are the receiver

Table 1
Description of pertinent CYGNSS data products.

CYGNSS data products	Description
Level 1	Normalized Bistatic Radar Cross-Section and Leading Edge Slope at the specular point with 25 km baseline resolution
Level 2	Surface wind speed in m/s at the specular point with 25 km baseline resolution
Level 3	Gridded surface wind speed for 0.2 × 0.2 (lat, lon) and temporal resolution of 60 min

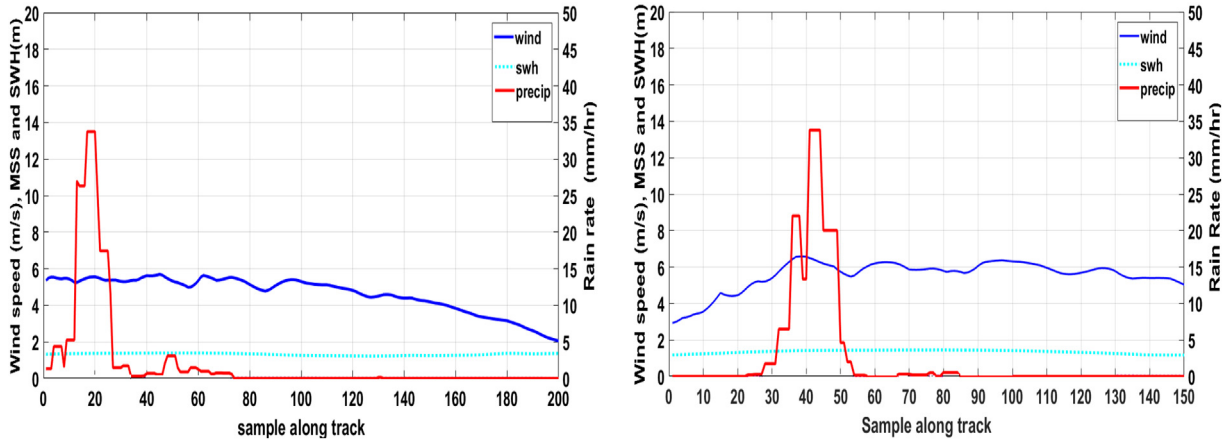


Fig. 8. Sample CYGNSS tracks in the controlled dataset. Along track precipitation in red and wind speed in blue and SWH in cyan. (For interpretation of the references to color in this figure legend, the reader is referred to the web version of this article.)

antenna gain and the incidence angle at the specular reflection point. For each member of the control dataset, all 4 of these control parameters are matched between the regions of strong-rain event and no-rain event. The no-rain event is a measurement sample on a given track where the precipitation is zero and peak rain event is the measurement along the same track but at the location of maximum precipitation. Thus, the pairs are matched on the same track between the strongest rain region and the nearest no-rain region, resulting in a total of 110 pairs of matchups. Fig. 8 depicts some of the tracks in the dataset. Note that the wind speed is fairly uniform across the entire track and the track contains both high precipitation and precipitation-free regions.

The control parameters in this dataset are shown in Fig. 9. The four control parameters are compared at the sample of peak precipitation and zero precipitation sample along the track. Note that all 4 parameters lie close to the 1:1 line, suggesting similar surface conditions and measurement geometry between the rain and no-rain regions. This reduces other potential sources of variation in the σ_0 and suggests that the observed differences in measured σ_0 between rain and no-rain conditions are most likely due to one or more of the 3 possible effects of rain.

3.3. Rain signature in CYGNSS wind retrieval

To extract rain signatures in the CYGNSS-GPM dataset, the pdf of all CYGNSS Level 3 wind retrievals globally is constructed for 2 different rain rate conditions. Fig. 10 shows the pdf for samples with a rain rate of < 5 mm/h and for samples with a rain rate of > 10 mm/h. We further randomly divide the sample population into 10 independent partitions of the dataset, with approximately 10^7 samples in each partition, and consider the distribution of their mean values. A significant difference in the mean of the distributions is evident between the two rain rate conditions. For samples with < 5 mm/h rain rate, the mean is ~7.4 m/s, which is consistent with global average wind speed. For the samples with > 10 mm/h rain rates, the mean is ~9.5 m/s, which indicates a significant shift in the measurements in the presence of rain.

3.4. Rain signature in σ_0 measurements

The increase observed in retrieved wind speed in the presence of rain might be due to actual increases in the wind that are associated with the rain or to changes in the surface roughness caused by rain that are misinterpreted as an increase in wind speed. To observe the impact of rain on the measurements, variations in σ_0 are examined.

Fig. 11 shows scatter plots from the complete matchup population amongst the three variables σ_0, wind speed and rain rate, with the abscissa being rain rate (left) or wind speed (right), the ordinate being σ_0 in each case, and the third variable sorted by color. In the right plot, a clear reduction in the magnitude of σ_0 is observed with increase in rain rates. Recall that attenuation of the signal due to rain is negligible below rain rates of 30 mm/h. This suggests that one or both of the other two phenomena, surface roughening due to rain and induced winds due to rain, are also associated with a decrease in σ_0. This behavior is examined in detail in the later sections. Note in both the plots that the dependence of σ_0 on rain rate becomes negligible above the range of 8–15 m/s. This suggests that the surface roughness due to wind dominates the effects of rain at wind speeds beyond the upper limit of 15 m/s. In the left plot, we observe the variation of σ_0 with rain rate for narrow wind speed bins. We can observe that σ_0 has a strong dependence on rain rate for wind speeds up to 5 m/s, a weaker dependence is visible up to 15 m/s, and above that there is no dependence observed.

3.5. Rain signature in direct DDM measurements

A double difference approach is taken to analyze the impact of rain on the CYGNSS DDMs. DDMs are modelled using the mission's End-to-End Simulator, which generates model DDMs for a given specified measurement geometry and an assumed wind speed (O'Brien et al., 2014). In this case, the wind speed used is the ECMWF matchup. The simulator assumes rain-free conditions. The difference between the observed and simulated DDMs is the first of two differences. The second difference is performed by considering a DDM at the point of maximum precipitation and a nearby one at zero precipitation along the same track. The double difference thus examines the difference between the ($obs - sim$) DDM with rain and without rain. The first difference

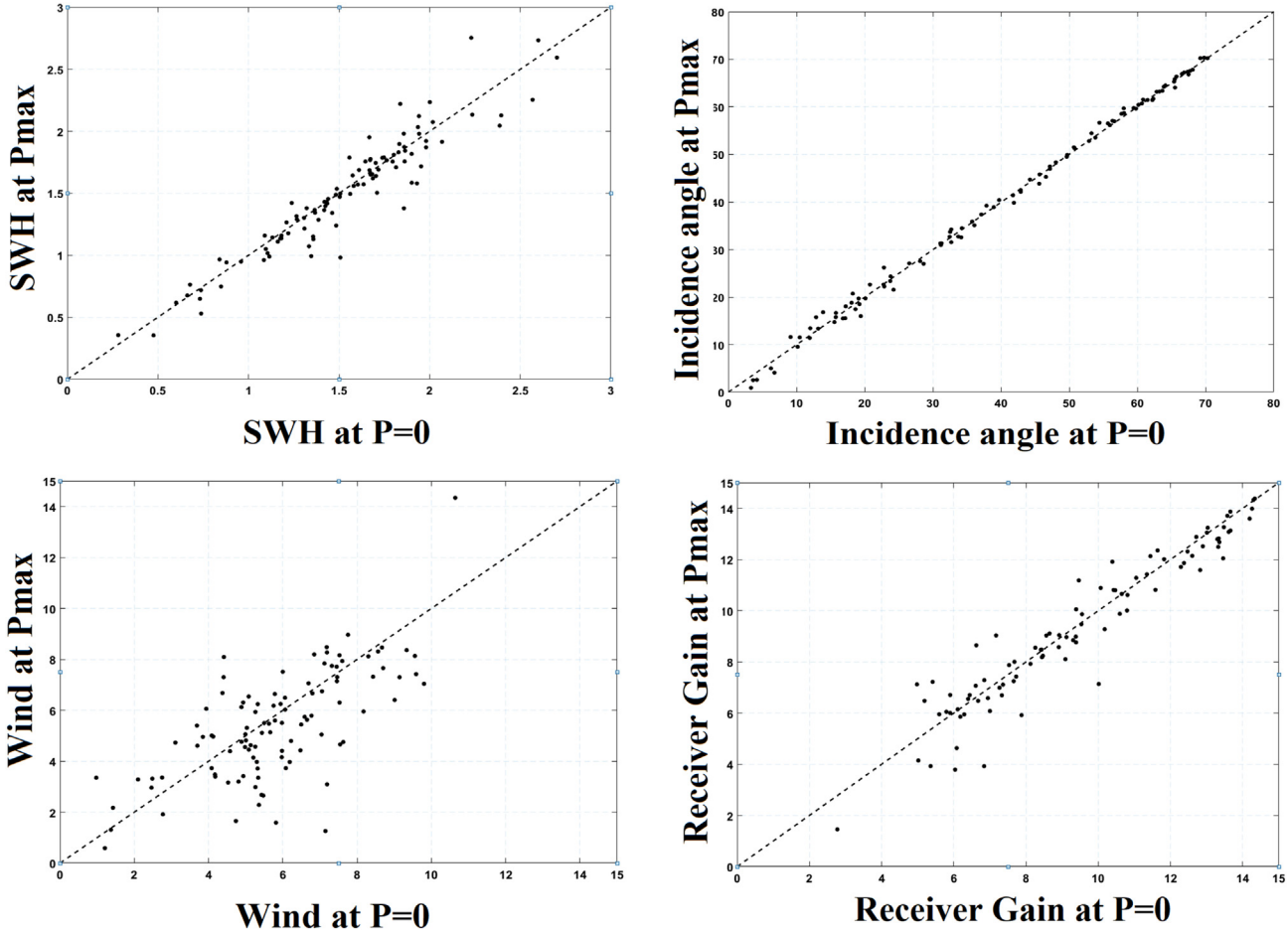


Fig. 9. Control parameters for controlled CYGNSS-GPM dataset.

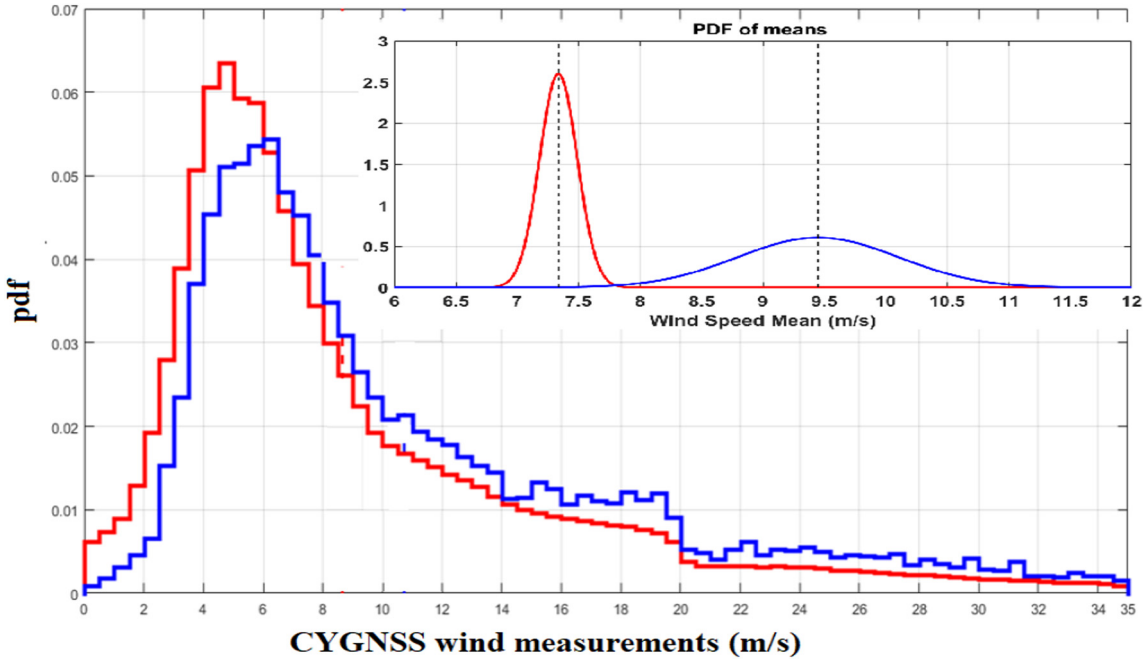


Fig. 10. PDF of CYGNSS wind retrievals for rain rates < 5 mm/h (red) and > 10 mm/h (blue). Top right: PDF of means of wind retrieval using 10 subsets of data for rain rates < 5 mm/h (red) and > 10 mm/h (blue). (For interpretation of the references to color in this figure legend, the reader is referred to the web version of this article.)

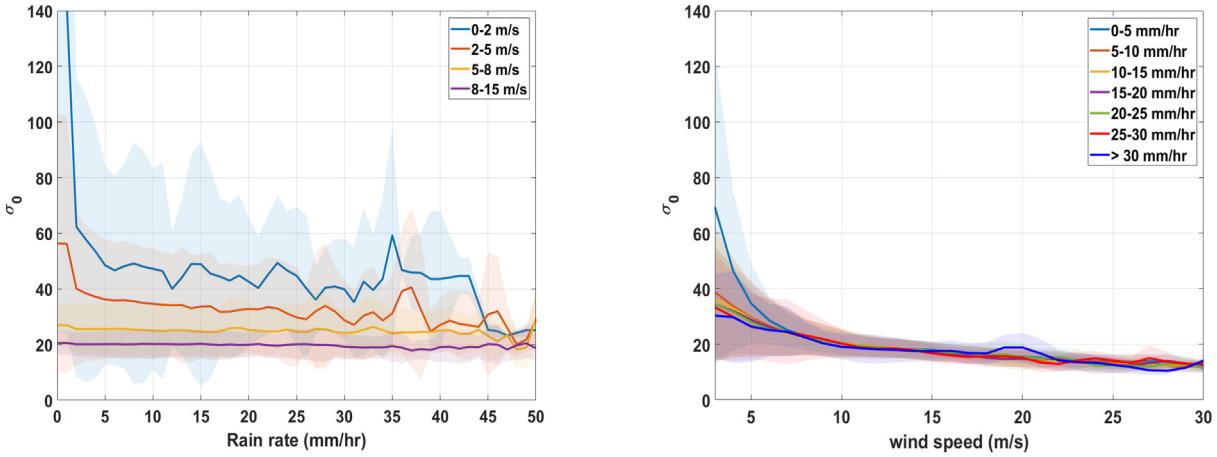


Fig. 11. (a) Variation in σ_0 with respect to rain for different ranges of wind speed. (b) Variation in σ_0 with respect to wind speed for different ranges of rain rate. (For interpretation of the references to color in this figure, the reader is referred to the web version of this article.)

accounts for possible offsets in the simulator and the second difference highlights the effects of rain. Note that the cases considered here feature only very small variations in either wind speed or measurement geometry along the track, in order to minimize the effects of all other surface and geometric parameters.

An example track is shown in Fig. 12. The image on the top left is a land mask with overlays showing the IMERG precipitation product by the color scale and the CYGNSS track in black. The red-x marks the CYGNSS sample at maximum precipitation and the green-x indicates the CYGNSS sample at zero precipitation. The double difference DDM method is performed at the 2 sample locations. The plot on the top right is the wind speed and precipitation information along the track. Note the wind speed drop at peak precipitation. We hypothesize that when the rain drops strike the surface, they suppress surface roughening associated with the wind. However, the falling rain also pushes down the air column, creating a downdraft which then flows radially outwards, creating higher winds outside the rain region. The bottom left image is the double difference DDM between peak-rain and no-rain events and the bottom right image is the double difference DDM for two adjacent no-rain samples. The DDMs shown are the DDM of power difference and their x-axis is the 11 Doppler bins and the y-axis is the 17 delay bins centered on the specular point.

The double difference DDM between peak-rain and no-rain events shows most of the difference in scattered power bins to be localized in the horseshoe region, with the highest difference near the specular point, suggesting that the rain information is concentrated near the specular point. The magnitude of this difference is comparable to the magnitude of the power received, which suggests that the effect of rain is not negligible. We see in the double difference between 2 no-rain samples (bottom right image) that the double-difference DDM has values close to zero everywhere. Fig. 13 shows the double difference DDM of power for 5 different CYGNSS tracks that has near uniform wind speed along the track. In all these cases, all the surface properties and geometries are very similar between peak rain and no rain region. This validates the assumption that the difference observed in the peak-rain vs no-rain case is caused by the presence of rain and most of the information is contained in the horse shoe region of the DDM.

4. Results

In the following sub-sections, we compare the CYGNSS observations to the proposed rain effect model to understand how well the model represents the underlying rain effects on ocean surface scattering of GPS signals.

4.1. Path integrated attenuation through rain

The integrated attenuation along the signal path is modelled in Eq. (7). We apply a loss correction to the measured of σ_0 to account for the drop in received power. The corrected σ_0 is denoted by $\sigma_0^{obs}|_R$. A perturbation model for the surface σ_0 can be written as:

$$\sigma_0^{obs}|_R = \sigma_0^{obs}|_{R=0} - \delta\sigma_0(R) \tag{11}$$

where $\sigma_0^{obs}|_{R=0}$ is the σ_0 (in linear scale) if there was no rain and $\delta\sigma_0(R)$ is the perturbation in σ_0 due to other effects of rain than attenuation which is assumed to be a function of rain rate.

The perturbation term is modelled empirically as follows: First, the CYGNSS-GPM matchups are obtained for a narrow range of wind speeds for the rain-free condition. Next, the attenuation corrected $\sigma_0^{obs}|_R$ is calculated based on the proposed model in Eq. (11) for different rain-rates. An empirical model for perturbation in σ_0 is then given by Eq. (12):

$$\delta\sigma_0(R) = < \sigma_0^{obs}|_{R=0} > + < \sigma_0^{obs}|_R > \tag{12}$$

where $< >$ denotes the expectation over a large population of CYGNSS Level 1 σ_0 values collected over 200 days in 2017. Thus, the rain induced surface roughening and increased surface winds due to rain are modelled as a difference in expectation of the σ_0 distribution for rain-free condition and the distribution of σ_0 at different rain rates.

The sample population for different rain rates is developed by filtering the CYGNSS-GPM matchup measurements by GPM IMERG rain rates. Fig. 14 shows the sample population density of CYGNSS samples at different rain rates.

To maintain the quality of estimation, we fix the threshold of number of samples per bin to be 10,000. The model developed for the σ_0 perturbation is of the form: Eq. (13)

$$\delta\sigma_0(R) = a^*R^b + c \tag{13}$$

where, a, b, and c are empirically derived coefficients and R is the rain rate in mm/ h. The model developed for the perturbation in σ_0 is shown in Fig. 15.

In the figure, note that the perturbation rises sharply for changes in rain rate from 0 to 15 mm/h and saturates at higher rain rates. This result is consistent with the observation in Fig. 11 (left), which shows that changes in the observed σ_0 are largest at rain rates below 15 mm/h and reduce at higher rain rates.

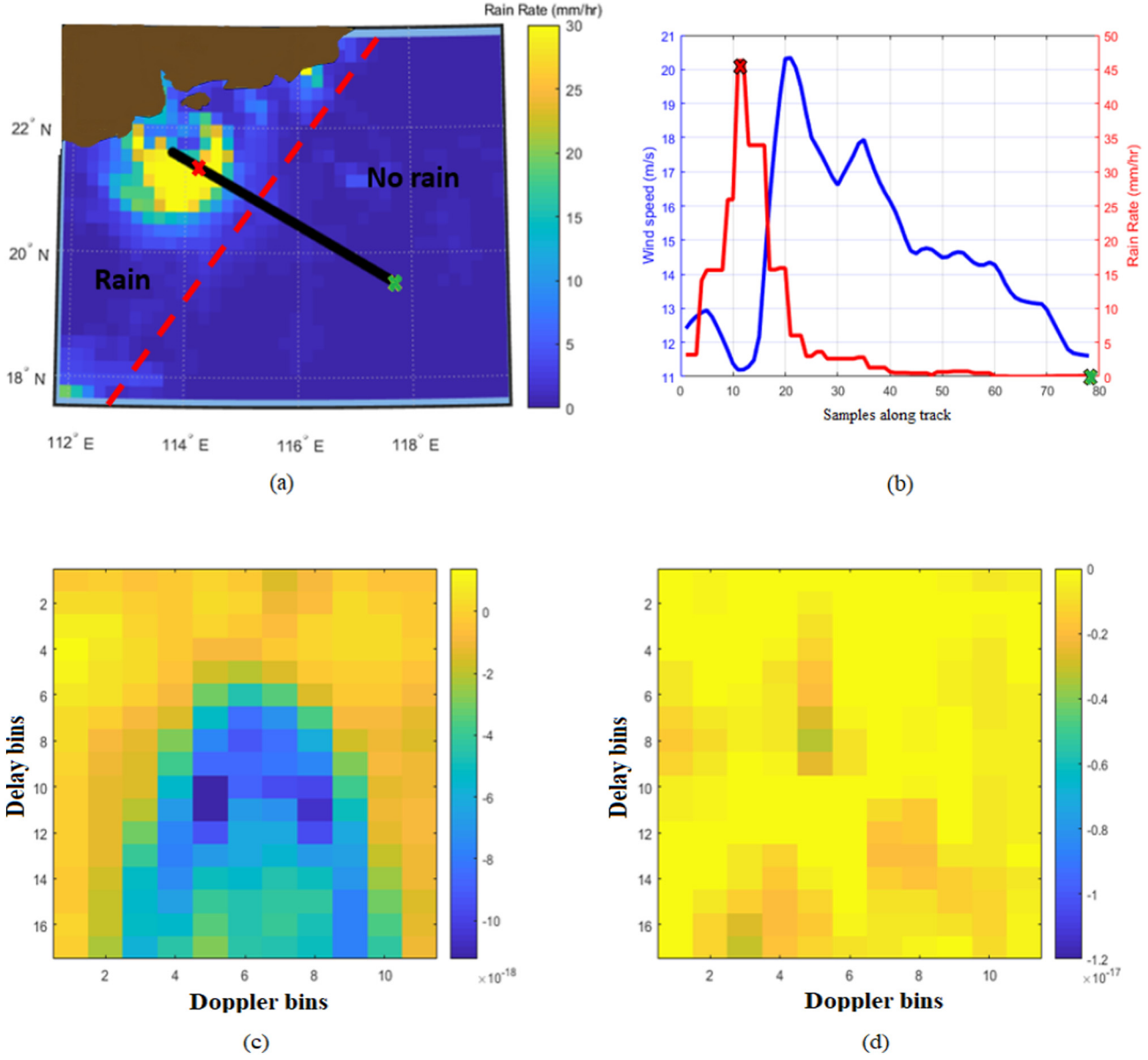


Fig. 12. Double difference DDM method for observing rain signature. (a) CYGNSS track overpass of a large convective rain cell (DOY 235, FM3, PRN 7). (b) Groundtruth ECMWF wind speed in m/s and GPM IMERG precipitation in mm/h along the track. (c) Double difference DDM of power in watts between a peak rain and a zero precipitation region. (d) Double difference DDM of power in Watts between 2 different zero precipitation regions. (For interpretation of the references to color in this figure, the reader is referred to the web version of this article.)

4.2. Ring-wave impact on roughness spectrum

A composite surface roughness spectrum is constructed using the Elfouhaily omnidirectional wind-wave spectrum together with the dominant ring-wave spectrum due to rain described above. The Mean Square Slope (MSS) at the surface is calculated from the composite spectrum by integration, as described by Elfouhaily et al. (1997), Eq. (14):

$$mss = \int_{k_{\min}}^{k_{\max}} k^2 S(k) dk \tag{14}$$

where k is wavenumber, $k_{\min}$ and $k_{\max}$ represent the limits of integration given by $k_{\min} = \frac{g}{10}\left(\frac{\Omega}{u_{10}}\right)^2$ and $k_{\max} = \frac{2\pi}{3\lambda}\cos(\theta)$, g is the acceleration due to gravity in m/s^2, Ω is the inverse wave age, u_{10} is the 10 m surface wind speed, λ is the wavelength of the transmit signal, θ is the incidence angle of the signal at the surface, and $S(k)$ is the composite roughness spectrum.

The expression for the upper limit of the integration, $k_{\max}$ is determined using the geometric optics limit and hence is only an approximate value. It is in the range of 10–12 rad/m at L-Band for typical angles of incidence. We consider here the possibility that the geometric optics approximation is not appropriate at sufficiently low wind speeds and levels of surface roughness, and that a different (higher) value for $k_{\max}$ may be more appropriate. The possibility is addressed empirically by comparing observed values of MSS to those predicted by the integral expression given by Eq. (14), while varying the assumed value of $k_{\max}$.

To illustrate our approach, consider an example surface with wind speed of 3 m/s and evaluate the MSS of this surface with no rain present and when additionally roughened by a rain rate $R = 100$ mm/ h. Fig. 16 shows the composite spectrum for a rain rate of 100 mm/h with the integration limits shown in red and blue. Note that the ring-wave portion of the spectrum is dominant only for $k > 50$ rad/m, but the low pass wavenumber ($k_{\max}$) is ~12 rad/m. The resulting MSS from Eq. (14) is 0.0111807484 for no rain ($R = 0$ mm/ h) and 0.01118119895 for a

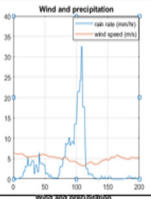
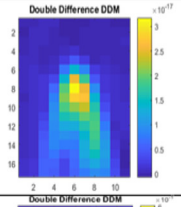
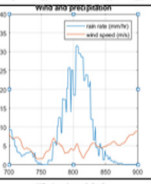
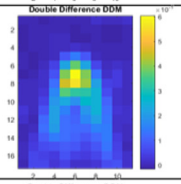
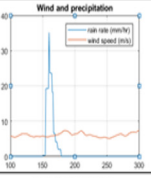
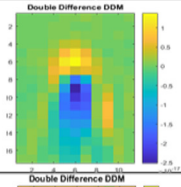
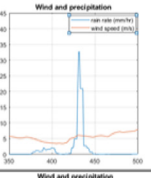
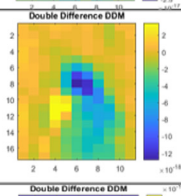
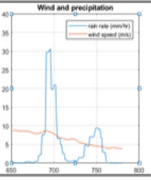
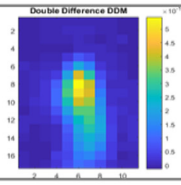
Precipitation	Wind speed	CYGNSS track	Double Difference DDM
Max P = 32.47 mm/hr Min P = 0 mm/hr	W at max P=3.39 m/s W at min P= 4.17 m/s		
Max P = 31.5 mm/hr Min P = 0 mm/hr	W at max P= 5.13 m/s W at min P= 5.66 m/s		
Max P = 35.13 mm/hr Min P = 0 mm/hr	W at max P= 5.59 m/s W at min P= 5. 78 m/s		
Max P = 32.63 mm/hr Min P = 0 mm/hr	W at max P= 6.0285 m/s W at min P= 6.0643 m/s		
Max P = 30.5 mm/hr Min P = 0 mm/hr	W at max P= 8.30 m/s W at min P= 8.56 m/s		

Fig. 13. Double difference DDM of power for 5 different CYGNSS tracks with near uniform wind along the track. Column 1: Precipitation information (P) at the peak and no precipitation sample points, Column 2: Wind information (W) at the peak and no precipitation sample points, Column 3: CYGNSS track with wind and precipitation information along the track and Column 4: Double difference DDM of power between the peak and no precipitation regions along the track.

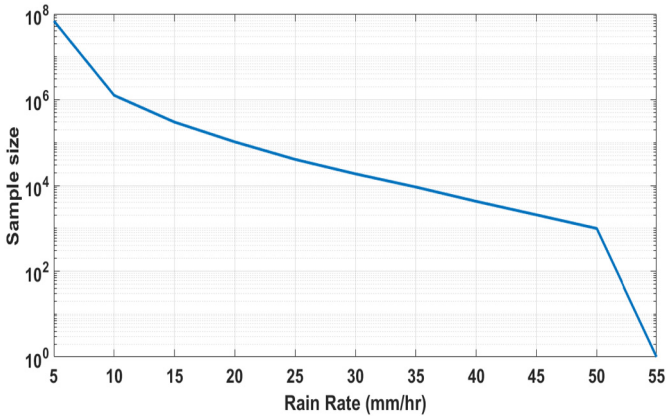


Fig. 14. CYGNSS samples for different rain rate bins.

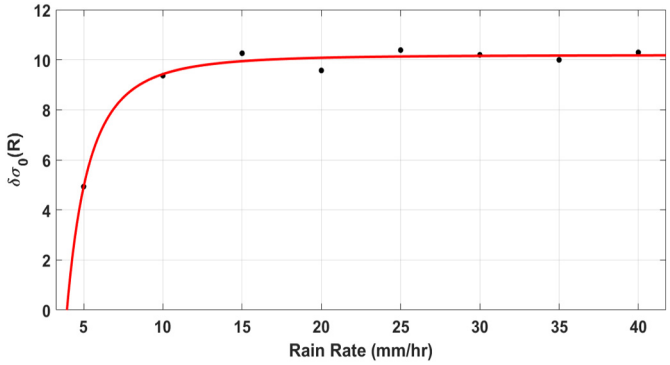


Fig. 15. Rain induces perturbation model.

rain rate of 100 mm/ h, or an increase of 0.004%. This suggests that the increase in MSS would be negligible at very high rain rates and low wind speeds, a model prediction which is not consistent with the behavior of the CYGNSS measurements. This motivates our consideration that the geometric optics limit for $k_{\max}$ may be underestimating the true low pass wavenumber.

Our empirical examination of $k_{\max}$ uses the controlled dataset of 110 CYGNSS tracks described above. An optimal low pass wavenumber is estimated by minimizing the absolute difference between the theoretical model for MSS and the MSS observed at the sample location of peak precipitation in the dataset. The optimal wavenumber is given by Eq. (15):

$$k_{opt} = \min_{k_{\max}} |mss_{model} - mss_{obs}| \tag{15}$$

An example is shown in Fig. 17 of the absolute difference as a function of $k_{\max}$. A distinct, global minimum in the absolute difference is evident at k_{opt}. This behavior of the absolute difference vs. $k_{\max}$ is consistent across all 110 tracks. The optimal low pass wavenumber tends to be slightly higher than the limit defined by the geometric optics

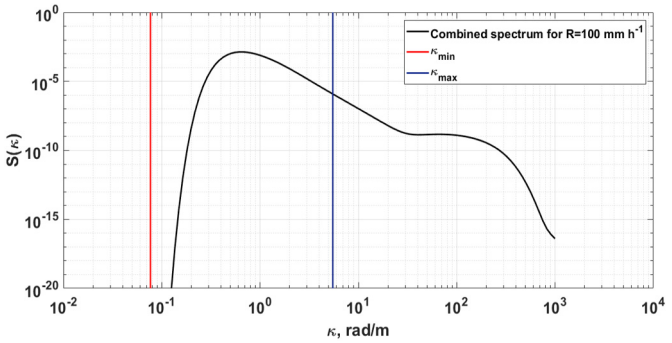


Fig. 16. Sample ocean surface roughness spectrum for wind speed = 3 m/s and rain rate = 100 mm/h. A rain-free roughness spectrum would decrease monotonically above $k \sim 0.6$ rad/m. The impact of rain causes a noticeable increase in roughness at $k = 50$–500 rad/m. (For interpretation of the references to color in this figure, the reader is referred to the web version of this article.)

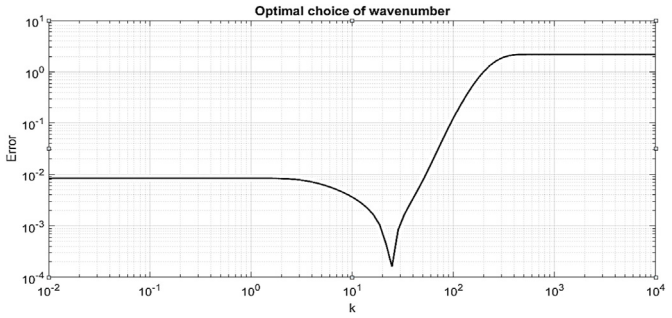


Fig. 17. Sample error minimization along track for optimal k.

approximation. k_{opt} is derived in this way for all the 110 tracks and is compared in Fig. 18 with the theoretical value for $k_{\max}$ in the geometric optics limit. Fig. 18a shows the theoretical value of $k_{\max}$ for each of the tracks. Averaging across all 110 cases, the mean low pass wavenumber from geometric optics is found to be 7.9486. Fig. 18b shows the value of k_{opt} for each of the 110 tracks.

In Fig. 18b, the optimal wavenumber is seen to vary as a function of wind speed, with its highest values close to 50 at very low wind speeds, and its value decreasing with increasing wind speed until if levels off at the mean geometric optics limit above ~5 m/s. A parametric model for k_{opt} as a function of wind speed, fit by least squares minimization to the 110 empirical values, is also shown in Fig. 18b. It is given by Eq. (16):

$$k_{maxnew} = k_0 + k_s{*}\exp\left(\frac{-u}{u_s}\right) \tag{16}$$

where k_{maxnew} is our new low pass wavenumber, k_0 is the geometric optics low pass wavenumber, ($k_s = 104.378$, $u_s = 0.7116$) are the empirical coefficients from the least squares minimization and u is the wind speed. We notice here that the new model for maximum wavenumber converges to the geometric optics limit above 5 m/s and retains its cosine dependence on incidence angle. However, this model suggests that the geometric optics limit breaks down at very low wind speeds, and it is under those conditions that the effects of surface roughening by rain become significant and measurable due to an increase in the upper bound of wavenumbers that affect the MSS. These results are consistent with the simulations of Voronovich and Zavorotny (2017) which show that the strong diffuse scattering approach to solving the bistatic radar equation inaccurately predicts the DDM for wind speeds < 5 m/s.

4.3. Comparison of downdraft winds with measurements

A model for the downdraft wind generated by rain was described above. We compare this model to observations by considering the surface wind speed in a rain-free area immediately adjacent to a rain event. One example CYGNSS track is shown in Fig. 19 with the regions of measurements highlighted that are used to calculate the downdraft wind speed. The x-axis represents the sample number along the track and the y-axis represents the parameters: wind speed, MSS, SWH and rain rate. The two black vertical lines show the region of rain-free measurement of wind speed on either side of the rain event, where precipitation is close to or identically zero. The observation of downdraft winds is defined as the average of wind measurements at the closest regions around the peak precipitation region where the rain rate is close to zero. This method of calculating the radial downdraft winds is equivalent to measuring radially outward-moving winds at 2 different locations along the track. These measurements are compared to the downdraft model-based winds which are evaluated by taking the rain rate as an input and solving the vertical momentum transfer equation to derive the radial downdraft winds as shown in Fig. 5. This procedure is followed for all the 110 tracks in the controlled CYGNSS dataset and the wind measurements are compared to the downdraft wind model shown in Fig. 7.

A typical rain event is usually much smaller and the rain rate value provided by the GPM IMERG level 3 product per grid and is likely not an accurate representation of the real situation. This is because the rain rate is not uniform within the grid cell. If a rain event occupies only 1/4th of the grid size it would lead to a lesser average rain rate in the grid than if the rain event occupies half or more in the grid cell. The IMERG rain product has a similar resolution as the CYGNSS sigma0 so this effect will be most significant if the relationship between the downdraft velocity and rain rate is non-linear, which is the case at lower rain rates as shown in Fig. 20.

However, the downdraft velocity at higher rain rates has a linear dependence on the rain rate (which is our region of interest) and hence the averaging effect of having non-uniform rain rates in the sub-grid space will have less of an impact.

The comparison of model and measurements is shown in Fig. 20. All the 110 tracks in the controlled CYGNSS dataset have a peak precipitation > 30 mm/ h. We observe that the model wind speed passes through the cluster of measurement points. There is considerable scatter between the model wind and the observations, which could be attributed to the simplified and approximate method used to calculate the downdraft wind from the rain rate. However, a general trend of increasing rain rate being accompanied by higher downdraft wind speed can be observed.

5. Discussion and conclusions

GNSS-R missions work on the principle of L-Band bistatic scatterometry. For accurate wind retrievals, it is important to understand the dominant rain effects at L-Band and how the σ_0 measurements are affected by them. In this work, we have identified 3 major effects of rain and have proposed a model for each. The observations used in this paper are from the CYGNSS constellation mission which is currently operational and has been collecting global ocean surface information since 2016.

The high-quality observation dataset encompasses a range of rain events with sufficient samples (> 10,000) up to a rain rate of 50 mm/ h. Using the CYGNSS measurements, a detailed empirical analysis was made to differentiate the effects caused by rain. The analysis suggests that: 1) the rain produces a reduction in magnitude of the measured σ_0 with increase in rain rate; and 2) the impact of rain can only be observed for wind speeds up to ~15 m/s.

The rain effect model proposed in this work has a 3-fold structure-path attenuation, modified surface roughness and downdraft winds. From the path attenuation model, we observe that the attenuation at L-Band due to raindrops is not significant, with transmissivity above 96% for rain rates below 30 mm/ h. After removing the effect of path

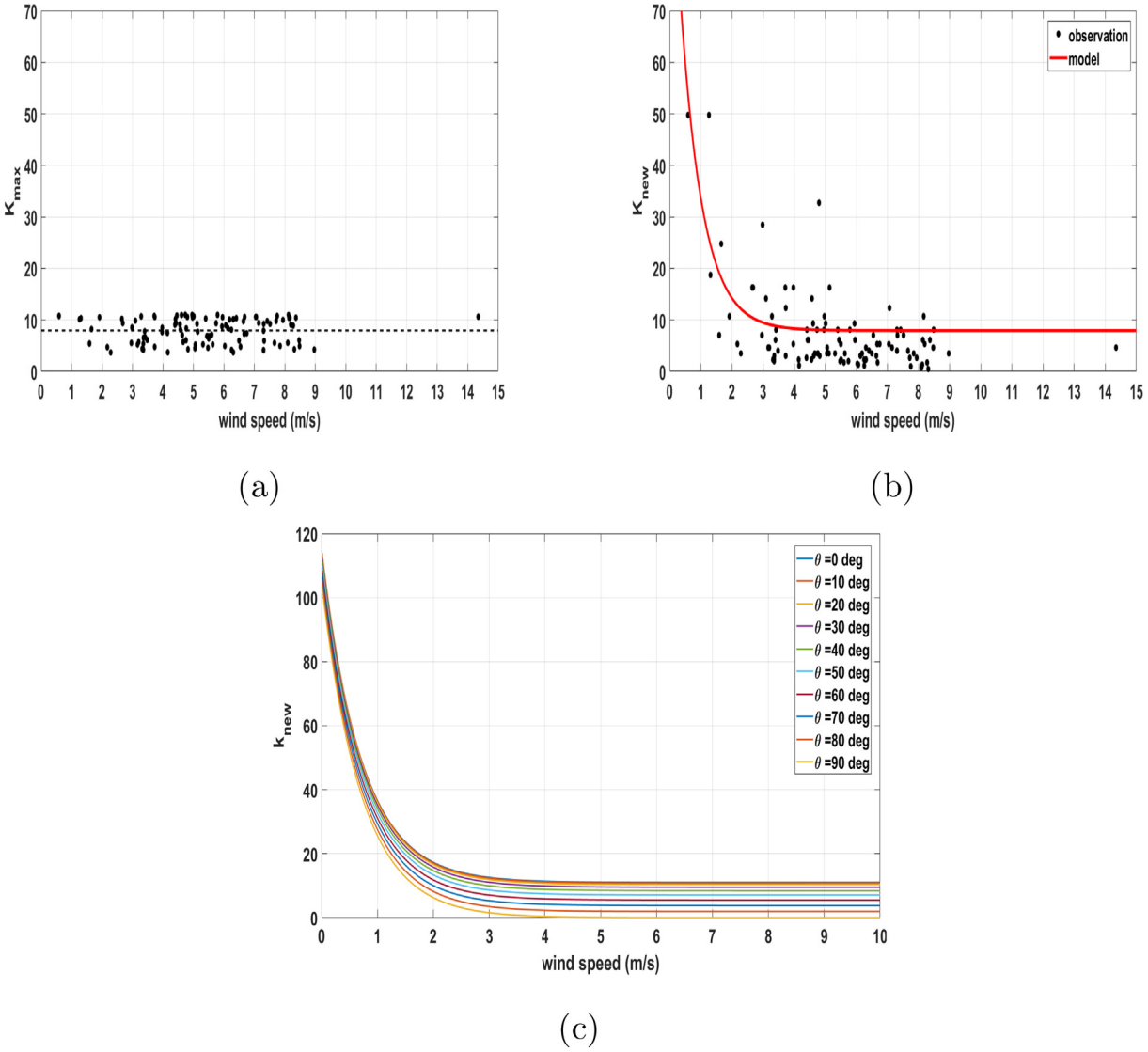


Fig. 18. (a) Theoretical maximum wavenumber (derived from geometric optics approximation), (b) optimal (empirically derived) maximum wavenumber of the surface roughness spectrum that significantly affects the mean squared slope and bistatic radar scattering cross-section, (c) A new maximum wavenumber model with wind speed and incidence angle dependence.

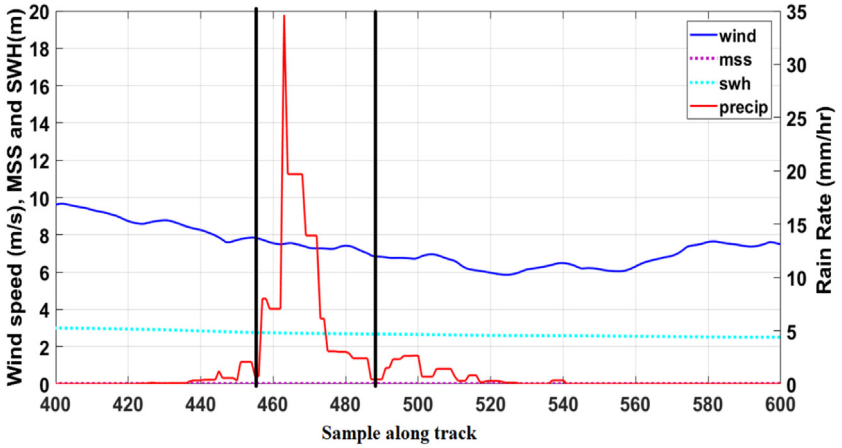


Fig. 19. Sample CYGNSS track measurement.

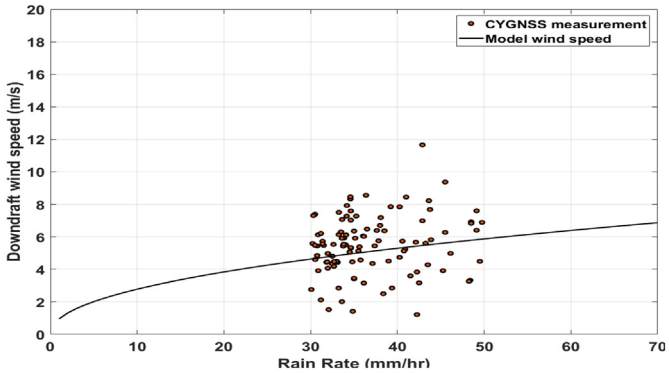


Fig. 20. Measurements over controlled dataset and model.

attenuation, the empirical model for perturbations in σ_0 sharply rises for a change in rain rate from 0 to 15 mm/h and saturates at higher rain rates. The model also shows that the perturbation in σ_0 is always negative, thus rain produces a drop in magnitude of σ_0.

The dynamic range of wind speeds is split into 2 regimes based on the electromagnetic scattering nature of the surface. The near specular regime is the region of wind speed < 5 m/s and above that is the diffuse scattering regime. In the near specular regime, we observe that the modified rain-wind roughness spectrum with a geometric optics approximation of the low pass wavenumber integration limit does not adequately account for the observed effects of rain. We empirically estimate the low pass wavenumber limit and determine that it is a function of wind speed. The limit of integration increases at very low wind speeds and saturates to the theoretical geometric optics limit for larger wind speeds (≥ 5 m/s). However, the net effect on a GNSS-R measurement at such low wind speeds is the combined effect of variation in the cut off wave number with wind speed as well as the coherent component in the forward scattering direction as shown in Voronovich and Zavorotny (2017).

The last of the 3 effects is local downdraft wind due to rain. Of the 3 different effects of rain studied in this work, we have found that the impact of attenuation is negligible and hence the total impact of rain on the measurements is dominated by the splash effect and the downdraft effect. Of these two, the splash effect is restricted to very low wind speeds (< 5 m/s) but the overall impact of rain can be observed up to surface wind speeds of 15 m /s. This suggests that the dominant effect on the moderate wind speed regime of 5–15 m/s is due to the downdraft effect. This model is compared to the simplified method of measuring the downdraft winds from the controlled dataset of 110 tracks. We find that the observation and the model are generally consistent in the estimation of downdraft winds and the model suggests that a maximum downdraft wind speed of 7 m/s should be present at very high rain rates.

CRediT authorship contribution statement

Rajeswari Balasubramaniam: Conceptualization, Methodology, Formal analysis, Investigation, Data curation, Writing - original draft, Writing - review & editing, Visualization. **Christopher Ruf:** Supervision, Conceptualization, Methodology, Writing - review & editing.

Declaration of competing interest

The authors declare that they have no known competing financial interests or personal relationships that could have appeared to influence the work reported in this paper.

Acknowledgements

The work presented was supported in part by NASA Science Mission Directorate contract NNL13AQ00C with the University of Michigan.

Appendix A. Relationship between downdraft winds and final velocity of falling rain drops

Following is a derivation from Holleman (2001) of the relationship between downdraft winds and the terminal velocity of a falling raindrop, which is used in this paper to understand the downdraft effect of rain on GNSS-R measurements.

The total vertical acceleration of an air parcel can be written using the vertical momentum equation as Eq. (A.1):

$$\frac{dw}{dt} \equiv \frac{\partial w}{\partial t} + w\frac{\partial w}{\partial z} \approx w\frac{\partial w}{\partial z} = \frac{1}{2}\frac{\partial w^2}{\partial z} \tag{A.1}$$

The time derivative can be neglected based on the assumption that the air parcel is stationary on the time scale of the downdraft. The effect of precipitation loading on the vertical motion of the air parcel is parameterized by the term gL, where g is the accelaration due to gravity and L is the precipitation mixing ratio (Emanuel, 1981; Wolfson, 1990; Doswell, 1994).

Downdraft wind velocity is defined as the vertical velocity at the surface (w_0) which is deflected by the surface in the horizontal direction. Let the downdraft start at height H above the surface, the velocity at the surface can be obtained from the integrated vertical momentum equation as given by Eq. (A.2):

$$\begin{aligned} &\frac{1}{2}\frac{\partial w^2}{\partial z} = -gL \\ &w^2(z) = 2g\int_0^H Ldz = \frac{2g}{\rho_0}\int_0^H H\rho_0 Ldz \\ &w^2(z) = \frac{2gMH}{\rho_0} = \frac{2gRH}{3600\rho_0 v_f} = 5.63\frac{RH}{v_f} \end{aligned} \tag{A.2}$$

where M is the precipitation loading per unit volume and ρ_0 is the vertically averaged air density. This averaged density is approximated as 0.968 kg/m^3, which is the value for a standard atmosphere between 0 and 5 km. The maximum downdraft velocity can therefore be written as Eq. (A.3):

$$w_0 = \sqrt{5.63\frac{RH}{v_f}} \tag{A.3}$$

Appendix B. CYGNSS controlled dataset

In this section, we describe the controlled dataset of 110 CYGNSS tracks used in the paper. Each track can be uniquely identified by the DOY (Day Of Year) for the year 2017, FM (CYGNSS satellite ID), PRN (GPS satellite ID) and time range. We have also added additional information such as location of peak precipitation regions and locations of downdraft points for each track Table B. 2. Each row is a CYGNSS track and has 9 fields: DOY, FM, PRN, time_upper (UTC secs), time_lower (UTC secs), loc_pmax, loc_pmin, loc_DDpt1, and locDDpt2. The details of these fields are given below: **DOY** — Day Of Year in 2017 **FM** — CYGNSS satellite ID **PRN** — GPS satellite ID **time_lower (UTC secs)** — the start time of the CYGNSS track at UTC time. **time_upper (UTC secs)** — end time of the CYGNSS track at UTC time. **loc_pmax** — sample location along track with max precipitation (1 is the starting sample of the track). **loc_pmin** — sample location along track with zero precipitation (1 is the starting sample of the track). **loc_DDpt1** — closest sample location to peak precipitation with minimum precipitation for first downdraft measurement (1 is the starting sample of the track). **loc_DDpt2** — closest sample location to peak precipitation with minimum precipitation for second downdraft measurement (1 is the starting sample of the track).

Table B. 2
Controlled CYGNSS dataset.

DOY	FM	PRN	time_lower (UTC secs)	time_upper (UTC secs)	loc_pmax	loc_pmin	loc_DDpt1	loc_DDpt2
168	8	25	33238	34107	108	138	73	115
168	3	25	33073	33912	281	244	256	291
164	4	8	11081	11948	362	408	359	371
159	8	18	7865	8874	23	80	4	41
155	2	24	46275	46904	581	498	567	589
146	4	25	30739	31588	332	372	298	360
145	5	12	23407	24636	352	390	323	381
145	3	12	23069	24338	381	421	351	408
144	6	19	40471	41100	94	119	84	111
143	6	12	72061	72730	297	320	278	304
143	6	25	77710	78339	327	359	313	344
142	7	19	41439	41998	17	74	3	27
142	6	25	78641	79210	271	296	258	283
142	5	19	41157	41756	41	58	31	52
140	4	25	81449	82128	211	184	197	233
140	1	21	60367	61046	58	95	46	77
138	5	17	4486	5225	450	494	431	464
135	8	29	57933	58302	133	192	122	142
135	5	20	58457	59206	435	411	425	444
133	1	10	45997	46826	646	703	641	656
133	1	31	12296	13335	279	373	272	287
124	1	22	46387	47356	804	877	767	839
124	1	18	21146	21975	99	79	88	164
122	4	19	67059	67838	695	664	685	710
121	3	12	31913	32652	443	423	436	461
121	1	12	31766	32475	440	404	414	452
120	3	3	61582	62591	160	150	154	174
118	8	22	30480	31379	345	301	320	384
118	1	7	57171	57615	285	364	275	331
117	2	24	32760	34099	796	776	786	818
105	1	15	32477	32706	59	112	51	78
102	2	14	58270	59019	444	413	437	488
264	4	8	36608	36957	37	27	34	48
263	5	12	46732	47501	54	16	41	72
262	6	17	53991	54760	146	195	129	179
262	4	24	46397	47126	651	637	646	660
262	3	24	75907	76452	431	468	425	437
261	5	10	54032	54801	216	237	212	229
258	3	17	10024	10522	95	143	81	112
258	2	17	10403	10802	169	212	151	184
257	1	8	4645	5284	356	375	353	262
255	3	29	29772	30501	227	259	203	236
254	6	17	15351	16150	364	377	345	372
253	6	23	30071	30930	393	371	381	410
252	1	32	62795	63714	230	268	223	243
251	2	10	58814	59673	500	518	490	507
249	7	21	7746	8685	359	393	315	372
248	7	21	48505	49184	246	270	225	264
247	2	24	43953	44482	367	407	354	385
245	6	21	32601	33380	154	180	124	171
245	4	8	27788	28597	89	113	85	103
245	2	2	28144	29023	189	225	147	211
243	3	13	35153	36771	637	672	613	650
237	3	27	43597	44682	527	540	512	534
232	4	11	12458	13037	151	206	134	188
231	8	10	15030	15189	91	72	84	109
231	6	10	14821	15010	93	78	83	107
231	3	25	58543	59242	266	239	259	316

(*continued on next page*)

Table B. 2 (*continued*)

DOY	FM	PRN	time_lower (UTC secs)	time_upper (UTC secs)	loc_pmax	loc_pmin	loc_DDpt1	loc_DDpt2
223	2	20	0	492	259	307	241	299
170	5	31	77832	78541	537	553	523	546
179	7	5	63187	63536	202	220	201	215
179	8	15	4062	4751	194	262	191	214
180	4	22	10199	10498	219	242	214	233
187	5	26	41267	42141	273	259	263	295
188	1	25	75265	76114	253	325	234	265
188	5	26	34131	34970	633	610	619	649
188	6	26	33773	34612	635	609	625	648
194	7	8	45471	46066	259	285	240	279
194	7	23	45067	45956	684	711	665	698
194	8	8	46074	46653	180	211	167	199
198	1	29	7350	8359	547	580	542	555
199	2	5	43554	44343	470	497	460	479
199	3	5	44332	44961	507	537	497	519
206	2	1	13224	14033	158	187	130	176
208	5	11	21802	22391	131	189	118	153
207	6	3	14375	15163	590	638	582	637
208	7	5	75456	76265	101	54	81	114
105	1	15	32477	32706	59	112	51	78
113	1	3	61757	62266	417	464	388	431
114	2	28	83691	84420	381	437	373	403
113	3	28	67783	68562	694	646	680	712
116	3	29	68753	70032	222	192	221	270
117	3	20	75653	76332	140	184	124	178
118	1	22	51607	52526	424	451	404	440
118	3	13	68833	69052	147	211	109	194
118	7	13	69369	70218	34	119	19	102
118	8	10	59339	59608	89	128	74	108
120	4	12	35378	36137	15	88	4	51
121	8	10	16780	17429	64	100	49	91
127	1	31	83627	84336	161	206	151	175
132	7	20	22559	23548	114	62	108	153
140	1	25	79667	80306	75	114	56	93
140	3	9	42618	43277	325	361	315	332
140	5	20	53587	54446	463	528	456	481
141	3	24	58359	58978	454	513	433	464
140	5	9	42736	43425	326	362	325	338
141	1	7	42437	42926	361	391	355	370
141	4	16	26399	27038	431	451	405	438
142	7	19	41439	41998	17	74	8	27
142	4	3	11449	12198	94	52	79	157
142	5	19	41157	41756	41	58	31	52
142	6	30	48101	48480	308	295	299	332
142	6	25	78641	79210	271	296	258	283
142	8	29	17544	18183	68	94	64	74
143	3	17	59748	60727	66	126	52	108
143	6	25	77710	78339	327	359	313	344
143	6	12	72061	72730	297	320	278	304
143	6	20	71801	72540	574	597	557	582
143	7	17	60168	61207	102	173	81	122
143	6	18	18201	19140	322	382	304	357

References

Asgarimehr, M., Zavorotny, V., Wickert, J., Reich, S., 2018. Can GNSS reflectometry detect precipitation over oceans? Geophys. Res. Lett. 45 (22), 12–585.

Asgarimehr, M., Wickert, J., Reich, S., 2019. Evaluating impact of rain attenuation on space-borne GNSS reflectometry wind speeds. Remote Sens. 11 (9), 1048.

Atlas, D., Ulbrich, C.W., 1977. Path-and area-integrated rainfall measurement by microwave attenuation in the 1–3 cm band. J. Appl. Meteorol. 16 (12), 1322–1331.

Balasubramaniam, R., Ruf, C.S., 2018. Improved calibration of CYGNSS measurements for downbursts in the Intertropical Convergence Zone. In: IGARSS 2018-2018 IEEE International Geoscience and Remote Sensing Symposium. IEEE, pp. 3987–3990.

Bass, F., Fuks, I., Kalmykov, A., Ostrovsky, I., Rosenberg, A., 1968. Very high frequency radiowave scattering by a disturbed sea surface part II: scattering from an actual sea surface. IEEE Trans. Antennas Propag. 16 (5), 560–568.

Bliven, L., Sobieski, P., Craeye, C., 1997. Rain generated ring-waves: measurements and modelling for remote sensing. Int. J. Remote Sens. 18 (1), 221–228.

Clarizia, M., Gommenginger, C., Gleason, S., Srokosz, M., Galdi, C., Di Bisceglie, M., 2009. Analysis of GNSS-R Delay-Doppler maps from the UK-DMC satellite over the ocean. Geophys. Res. Lett. 36 (2).

Contreras, R.F., Plant, W.J., 2006. Surface effect of rain on microwave backscatter from the ocean: measurements and modeling. J. Geophys. Res. Oceans 111 (C8).

Craeye, C., Sobieski, P., Bliven, L., 1997. Scattering by artificial wind and rain roughened water surfaces at oblique incidences. Int. J. Remote Sens. 18 (10), 2241–2246.

Doswell, C., 1994. Extreme convective windstorms: current understanding and research. In: Report of the Proceedings of the US-Spain Workshop on Natural Hazards (Barcelona, Spain, 8–11 June 1993), pp. 44–55.

Doviak, R.J., et al., 2006. Doppler Radar and Weather Observations. Courier Corporation.

Draper, D.W., Long, D.G., 2004. Simultaneous wind and rain retrieval using SeaWinds data. IEEE Trans. Geosci. Remote Sens. 42 (7), 1411–1423.

Elfouhaily, T., Chapron, B., Katsaros, K., Vandemark, D., 1997. A unified directional spectrum for long and short wind-driven waves. J. Geophys. Res. Oceans 102 (C7), 15781–15796.

Emanuel, K.A., 1981. A similarity theory for unsaturated downdrafts within clouds. J. Atmos. Sci. 38 (8), 1541–1557.

Foti, G., Gommenginger, C., Jales, P., Unwin, M., Shaw, A., Robertson, C., Rosello, J., 2015. Spaceborne GNSS reflectometry for ocean winds: first results from the UK TechDemoSat-1 mission. Geophys. Res. Lett. 42 (13), 5435–5441.

Ghavidel, A., Camps, A., 2016. Impact of rain, swell, and surface currents on the electromagnetic bias in GNSS-Reflectometry. IEEE J. Sel. Top. Appl. Earth Obs. Remote Sens. 9 (10), 4643–4649.

Harris Jr, G.N., Bowman, K.P., Shin, D.-B., 2000. Comparison of freezing-level altitudes from the NCEP reanalysis with TRMM precipitation radar brightband data. J. Clim. 13 (23), 4137–4148.

Holleman, I., 2001. Estimation of the maximum velocity of convective wind gusts. In: Internal KNMI Report.
Huffman, G.J., Bolvin, D.T., Braithwaite, D., Hsu, K., Joyce, R., Xie, P., Yoo, S.-H., 2015. NASA Global Precipitation Measurement (GPM) Integrated Multi-satellitE Retrievals for GPM (IMERG). In: Algorithm Theoretical Basis Document, version 4, pp. 30.
Marshall, Palmer, Mc.K., 1948. The distribution of raindrops with size. J. Meteorol. 5, 165–166.
Nielsen, S.N., Long, D.G., 2008. A wind and rain backscatter model derived from AMSR and SeaWinds data. IEEE Trans. Geosci. Remote Sens. 47 (6), 1595–1606.
O'Brien, A., Gleason, S., Johnson, J., Ruf, C., 2014. The End-to-End simulator for the Cyclone GNSS (CYGNSS) mission. IEEE J. Sel. Topics Appl. Earth Obs.
Ruf, C.S., Balasubramaniam, R., 2018. Development of the CYGNSS Geophysical Model Function for wind speed. IEEE J. Sel. Top. Appl. Earth Obs. Remote Sens. (99), 1–12.
Ruf, C., Unwin, M., Dickinson, J., Rose, R., Rose, D., Vincent, M., Lyons, A., 2013. CYGNSS: enabling the future of hurricane prediction [remote sensing satellites]. IEEE Geosci. Remote Sens. Mag. 1 (2), 52–67.
Ruf, C., Chang, P., Clarizia, M., Gleason, S., Jelenak, Z., Murray, J., Morris, M., Musko, S., Posselt, D., Provost, D., et al., 2016. CYGNSS Handbook. http://clasp-research.engin.umich.edu/missions/cygnss/reference/cygnss-mission/CYGNSS_Handbook_April2016.pdf.
Ruf, C.S., Chew, C., Lang, T., Morris, M.G., Nave, K., Ridley, A., Balasubramaniam, R., 2018. A new paradigm in earth environmental monitoring with the CYGNSS small satellite constellation. Sci. Rep. 8 (1), 8782.
Soisuvarn, S., Jelenak, Z., Said, F., Chang, P.S., Egido, A., 2016. The GNSS-reflectometry response to the ocean surface winds and waves. IEEE J. Sel. Top. Appl. Earth Obs. Remote Sens. 9 (10), 4678–4699.
Stiles, B.W., Yueh, S.H., 2002. Impact of rain on spaceborne Ku-band wind scatterometer data. IEEE Trans. Geosci. Remote Sens. 40 (9), 1973–1983.
Tang, W., Yueh, S., Fore, A., Neumann, G., Hayashi, A., Lagerloef, G., 2013. The rain effect on Aquarius' L-band sea surface brightness temperature and radar backscatter. Remote Sens. Environ. 137, 147–157.
Tang, W., Yueh, S.H., Hayashi, A., Fore, A.G., Jones, W.L., Santos-Garcia, A., Jacob, M.M., 2015. Rain-induced near surface salinity stratification and rain roughness correction for Aquarius SSS retrieval. IEEE J. Sel. Top. Appl. Earth Obs. Remote Sens. 8 (12), 5474–5484.
Ulaby, F.T., Long, D.G., Blackwell, W.J., Elachi, C., Fung, A.K., Ruf, C., Sarabandi, K., Zebker, H.A., Van Zyl, J., 2014. Microwave Radar and Radiometric Remote Sensing. vol. 4 University of Michigan Press, Ann Arbor.
Voronovich, A.G., Zavorotny, V.U., 2017. Bistatic radar equation for signals of opportunity revisited. IEEE Trans. Geosci. Remote Sens. 56 (4), 1959–1968.
Weissman, D., Stiles, B., Hristova-Veleva, S., Long, D., Smith, D., Hilburn, K., Jones, W., 2012. Challenges to satellite sensors of ocean winds: addressing precipitation effects. J. Atmos. Ocean. Technol. 29 (3), 356–374.
Wetzel, L., 1990. On the theory of electromagnetic scattering from a raindrop splash. Radio Sci. 25 (06), 1183–1197.
Wolfson, M.M., 1990. Understanding and Predicting Microbursts. Ph.D. thesis. Massachusetts Institute of Technology.
Xu, F., Li, X., Wang, P., Yang, J., Pichel, W.G., Jin, Y.-Q., 2014. A backscattering model of rainfall over rough sea surface for Synthetic Aperture Radar. IEEE Trans. Geosci. Remote Sens. 53 (6), 3042–3054.
Zavorotny, V.U., Voronovich, A.G., 2000. Scattering of GPS signals from the ocean with wind remote sensing application. IEEE Trans. Geosci. Remote Sens. 38 (2), 951–964.
Zavorotny, V., Voronovich, A., 2018. GNSS-R modeling results obtained with improved bistatic radar equation. In: 2018 International Conference on Electromagnetics in Advanced Applications (ICEAA). IEEE, pp. 35–38.
Zhang, G., Li, X., Perrie, W., Zhang, B., Wang, L., 2016. Rain effects on the hurricane observations over the ocean by C-band Synthetic Aperture Radar. J. Geophys. Res. Oceans 121 (1), 14–26.